Improving the High-Temperature Mechanical Properties of L-PBF CM247LC Through HIPing and Aging Treatments

SUYALATU,KAZUTO ARAKAWA, HIDEKI WAKABAYASHI, SHOHEI UEKI, NORIO HIGUCHI, HITOSHI SAKAI, YUGO HIGASHIDA, D. GRAHAM MCCARTNEY, CATHERINE RAE, and ROGER C. REED

CM247LC was fabricated using L-PBF with optimized build parameters to minimize cracking. This paper explores the potential for using HIPing, followed directly by aging heat treatments, to optimize tensile and creep properties while reducing the number of heat treatments and the cost of processing. Samples were HIPed at 1250 °C and 100 MPa followed by aging treatments chosen to replicate those given to the DS alloy after solutioning. Heat treatments at 1250 °C, both the furnace only and HIP, have similar effects on grain structure, but change γ' morphology. The slow cool following HIPing results in large (~2 μm) octo-dendritic primary γ', and the subsequent anneals have radically different effects on the microstructure. The best tensile performance at 900 °C is produced by minimizing the volume fraction of primary γ' during the anneal at 1080 °C and peak-aging the secondary γ', formed during the cool from 1080 °C, and aging at 870 °C. Creep tests at 982 °C and 179 MPa show that the HIP treatment is essential to prevent early failure. It is remarkable that the optimum tensile microstructure performs well in creep despite large primary γ'. Omitting a separate solution treatment gives a radically different microstructure but tensile properties that match those from the cast alloy, without compromising the creep performance at low strain.

https://doi.org/10.1007/s11661-025-08106-7

I. INTRODUCTION

OVER the last decade, there has been enormous interest in additive manufacturing (AM) methods such as laser powder bed fusion (L-PBF) and direct energy deposition (DED) for the production of metallic parts. L-PBF, involving layer-by-layer deposition through the selective melting of metallic powder particles using a high-power laser beam scanned across a powder bed, is particularly attractive for complex three-dimensional components. Therefore, L-PBF offers considerable potential for the manufacture of nickel-based superalloys for high-temperature applications in gas turbines, where advantage could be taken of the high dimensional accuracy, reduced scrappage, and greater design freedom. Industry adoption of AM has steadily increased across aerospace sectors and has been implemented for various components, such as gas turbine fuel nozzles, burner tips, smaller aircraft engines, and rocket engine.[1]

However, a significant challenge with the L-PBF of γ'-strengthened Ni-based superalloys is their high susceptibility to cracking during processing. Several different types of solidification and solid-state cracking mechanisms are observed during the deposition of this type of superalloy, which have been documented extensively in recent years.[2–6] Much research continues to understand the fundamentals of cracking mechanisms and to find suitable approaches to eliminate these defects. For example, an emerging area of research has focused on using the alloys by design (ABD) approach to design alloys with improved overall processability while maintaining sufficient γ' content for good

SUYALATU, NORIO HIGUCHI, and HITOSHI SAKAI are with the NTT Data XAM Technologies Corporation, Osaka, Japan. Contact email: suyalatu@nttdata-xam.com KAZUTO ARAKAWA, HIDEKI WAKABAYASHI, and SHOHEI UEKI are with the NEXTA Centre, Shimane University, Matsue, Japan. YUGO HIGASHIDA is with the NTT Data XAM Technologies Corporation and also with the Kiguchi Technics Inc., Yasugi, Japan. D. GRAHAM MCCARTNEY, and ROGER C. REED are with the NEXTA Centre, Shimane University and also with the Department of Materials, Oxford University, Oxford, UK. CATHERINE RAE is with the NEXTA Centre, Shimane University and also with the Department of Materials Science and Metallurgy, Cambridge University, Cambridge, UK.
Manuscript submitted October 3, 2025; accepted December 30, 2025.

Published online: 20 January 2026

mechanical properties at high temperatures and stresses.[7] Conversely, there has been considerable work reported on avoiding cracking in γ'-strengthened heritage alloys such as IN939, Inconel700 and CM247[8] that are traditionally difficult to weld using a process optimization approach.[9] Many studies have reported results on the effect of modifying laser scan strategies and optimizing parameter selections, but challenges remain in applying findings from small scale builds (typically cubes) to component-scale geometries.

It has been of particular interest to improve the processability by L-PBF of the high γ' volume fraction (~65 vol pct), high strength alloy CM247LC. This was originally developed for the manufacture of high-temperature gas turbine components such as turbine blades and vanes by directional solidification (DS) and is a slightly modified version of CM247 with a lower carbon content and tighter controls on the elements Si and S in order to reduce its susceptibility to cracking during DS.[10] It is well established that, following L-PBF, CM247LC typically solidifies with a strong [001] columnar grain texture along the build direction and has a fine scale cellular-dendritic solidification morphology within the columnar grains.[11] However, cracking is commonly seen in the as-built condition and the various cracking sub-types, namely solidification cracking, liquation cracking and solid-state cracking, have been widely studied and reported.[3,4,8,11–13] It is accepted that contributory factors to the cracking susceptibility of CM247LC include the following: its wide freezing range (100–120 K)[2,13]; solute segregation and intercellular carbide precipitation due to the alloy chemistry and non-equilibrium solidification; and the high residual stresses that result from the rapid cooling rates (~10^6 Ks^{-1}) and large thermal gradients that are features of the L-PBF process. Safety critical, load-bearing parts made by L-PBF for gas turbines must be free from cracks to ensure structural integrity and mechanical reliability under service conditions. Therefore, investigations of laser parameters (laser power, scan speed, hatch distance, scan strategy) and other processing parameters have been undertaken to optimize the critical characteristics of L-PBF builds and minimize cracking.[3] More recently, highly customized strategies, including the use of multi-laser machines and pulsed power profiles, are being developed. However, despite extensive research efforts on process modifications, CM247LC cracks cannot be eliminated entirely from within the L-PBF process.

Thus, it has become necessary to consider the use of post-fabrication processing to close up or heal cracks in the as-built structure. Carter *et al.*[3,4] were one of the first to propose and investigate the use of hot isostatic pressing (HIPing) as a post-fabrication treatment. HIPing involves the simultaneous application of high pressure, usually via an inert gas, and an elevated temperature in a sealed vessel. Under appropriate conditions, internal defects inside a solid, not connected to the free surface, collapse and weld. Key parameters in HIPing are the peak temperature and pressure with the sample, as well as the heating and cooling rates. Carter *et al.*[3] found that HIPing of CM247LC was effective at closing the remaining internal cracks, and this post-fabrication route has been investigated in more detail by several other researchers. Lee *et al.*[14] also found that HIPing was effective in closing cracks. They observed no change in grain structure under their HIPing conditions, but found significant changes in γ' morphology and an improvement in room-temperature tensile properties. Bassini *et al.*[15] also assessed the microstructure of CM247LC after HIPing and following a post-HIP solution treatment at 1245 °C and single-step aging. They observed that the combined effect of the solution and first aging treatments modified the as-built grain structure and significantly altered the γ' precipitation. However, it has been reported[16] that HIP is less effective for crack healing above a threshold crack width of ~ 6 μm, emphasizing the importance of selecting appropriate L-PBF parameters to control prior crack dimensions. Markanday *et al.*[11] systematically investigated the microstructure evolution of CM247LC through a series of post-deposition processing steps which included HIPing followed by solution treatment both at 1250 °C and single-step aging at 870 °C. They observed crack healing after HIPing but their post-processing regime was not optimized with only a partially recrystallized grain structure and a non-homogenous morphology and distribution of γ' precipitate.

Although HIPing appears to offer significant potential as a post-processing stage to eliminate cracking, most researchers to date have proposed that HIPing must be followed by a separate solution treatment at ~ 1250 °C introducing a substantial additional processing cost. Therefore, further research is needed to investigate whether it is feasible to employ HIPing and aging conditions that eliminate the solution treatment and achieve the desired high-temperature mechanical properties. While Martelli *et al.*,[17] Carter,[4] and Fardan[18] have explored this approach, their work involved HIP equipment that cooled samples at high rates (160, 2450, and 250 K min^{-1}) and a single-step age. However, industrial practice typically involves HIP heating/cooling rates of 5–20 K min^{-1}. Similarly, Fardan *et al.*[18] looked at combined HIPing and solution treatments at 1250 °C and 1280 °C with a cooling rate of 250 K min^{-1} cycle and found an advantage in creep from the larger grain size from the higher temperature.

The main purpose of the work reported here was to investigate the potential for using the HIPing stage as a solution treatment, followed directly by a two-step aging heat treatment to control γ' formation. The relationship between the tensile and creep properties of CM247LC and the novel bimodal γ' distributions formed were studied, and transmission electron microscopy was employed to reveal the interactions between dislocations and γ/γ' features.

II. EXPERIMENTAL METHODS

A. *Alloy Composition and Heat Treatments*

The CM247LC powder used in this study has a spherical morphology with an average powder size dimension of 30.15 μm, and a chemical composition, as determined by ICP analysis and LECO analysis (O, N, C), given in Table I.

Five distinct sample geometries were produced in an Ar atmosphere using the Eosint M290 manufactured by EOS GmbH. These were: 10 mm cubes for microstructural analysis; Z tensile samples of gauge diameter 6.2 mm and length 32 mm and 46 mm; XY tensile samples: $8 \times 8 \times 32$ mm and $8 \times 8 \times 46$ mm. These are shown in Fig S-1 of supplementary material. In this paper, the build direction is the Z-axis and the transverse plane is the XY plane. All samples were manufactured using process parameters previously optimized using the 10 mm cubes to produce minimal density of pores and cracks. Crack density is a function of laser power, scan speed, and scan spacing expressed as energy density.[16] Carter shows a decrease in crack density with scan speed and with laser power, and a more complex dependence on scan spacing. These studies show that provided sufficient energy is supplied to fully melt the material, reducing the energy input tends to decrease cracking. These principles were followed to produce the virtually crack-free material used in this work. Micrographs of the as-built material and its precursors are included as Figure S-2 of supplementary material.

To eliminate any residual defects and control the microstructures, hot isostatic pressing (HIPing) was performed for 2 hour at a pressure of 100 MPa and a temperature of 1250 °C (heating rate of 6.7 K min^{-1}). The furnace cooled at around 13.3 K min^{-1} and pressure was released at 280 °C. All samples were machined after HIP, solution treatment, and aging.

Heat treatments of the mechanical samples were carried out in a vacuum furnace (FT-01VAC-1650), at a pressure of 3×10^{-1} Pa. Following heat treatment, samples were exposed to air, removed through the furnace window, placed on an Inconel plate at room temperature, and cooled with a forced gas quench. The double aging conditions applied to both HIPed and non-HIPed samples were chosen to mirror those used for cast CM247LC. The non-HIPed samples were solutioned at 1220 °C and 1250 °C and the cooling rate estimated to be at least 300 K min^{-1}. Following solution treatment, non-HIPed samples were annealed at 1080 °C for 4 hour and 870 °C for 20 hour. Following HIP, the aging treatment was carried out at 1080 °C for 0, 2 or 4 hours, followed by aging at 870 °C for 0, 10 or 15 hours.

B. *Materials' Characterization*

The microstructure was examined for grain configuration, texture, carbide, and γ' morphology in the as-manufactured, HIPed, and HIPed plus heat-treated 10 mm cube samples. Slices of the 10 mm cubes, 0.5 mm thick, were ground until 1000# paper, diamond polished at 9 and 3 μm, and finished with OPS polishing. To observe the γ' size, distribution, and morphology, samples were electrolytically etched to remove the γ matrix using 10 pct perchloric acid in methanol at 15–20 V and − 30 °C to − 20 °C. The γ' sizes were measured using ImageJ software. The volume fraction of primary γ' was obtained by analyzing images taken using an optical microscope, VHX-8000 (Ver. 2.242.271), from Keyence corporation. An area of 18.3×13.7 μm was examined at a magnification of 7 k. The volume fraction of secondary γ' was obtained by analyzing images of size 8.53×6.4 μm at 15 k magnification taken with the FEGSEM. This is about five times the areas shown in Figure 3 and includes about 150 primary γ' precipitates.

A Zeiss Merlin Gemini 2 Field Emission Gun Scanning Electron Microscope (FEGSEM) equipped with an Oxford Instruments X-Max energy-dispersive detector and an electron backscattered diffraction (EBSD) system was used for most investigations. Imaging of etched samples used backscattered electron and secondary electron imaging, and energy-dispersive X-ray spectroscopy (EDX) maps were acquired using an accelerating voltage of 10 kV and probe current of 500 pA.

Further electron backscattered diffraction (EBSD) analyses were conducted using a JEOL JSM-IT-800 FEGSEM equipped with TSL OIM Data collection 7 EBSD system at an acceleration voltage of 15 kV and with a probe current of 100 pA for scanning electron microscopy and 7 nA for EBSD analysis. Energy-dispersive X-ray spectroscopy (EDX) was also conducted on JEOL JIB-4700F FEGSEM equipped with Oxford Instruments Ultim Max EDX system with an acceleration voltage of 15 kV and probe current of 1 nA

Transmission electron microscopy (TEM) was conducted on a JEOL NEO-ARM equipped with an EDX detector at an acceleration voltage of 200 kV for scanning transmission electron microscopy (STEM), high-angle annular dark field (HAADF) imaging, and STEM-EDX elemental mapping. Further, TEM

Table I. Chemical Composition (Mass Pct) of the As-received Powder Supplied by Praxair

Element	C	Cr	Co	W	Mo	Ta	Al	Ti	Hf	B	Zr	Ni	O	N
Result	0.07	8.3	9.4	9.6	0.5	3.2	5.6	0.8	1.6	0.02	0.02	bal	0.02	0.00
Min	0.05	8.0	9.0	9.3	0.4	3.1	5.4	0.6	1.2	0.01	0.004	bal		
Max	0.1	8.5	9.5	9.7	0.6	3.3	5.7	0.9	1.6	0.03	0.02	bal		

imaging of dislocations in deformed samples was conducted on a JEOL JEM-2010 microscope with a high-contrast objective lens pole piece operating at 200 kV. Samples were polished by grinding to 0.1-0.13 mm in thickness, diamond polishing at 9 and 3 μm, and finished with OPS polishing. These samples were perforated by electropolishing in a solution of 10 pct perchloric acid in methanol at voltage 10–20 V and temperature − 30 °C to − 20 °C in a twinjet polishing machine.

C. *Mechanical Testing*

1. *Uniaxial tensile tests*

Isothermal uniaxial tensile tests were performed using an INSTRON5982 equipped with a 100 kN load cell to standard ASTM E8/E8M. Specimens of length of 32 mm, diameter of 5 mm, gauge length of 10 mm, and gauge diameter of 2.5 mm were machined from the fully heat-treated material by wire Electrical Discharge Machining (EDM), and polished to Ra 0.8 μm finish using 240 grit SiC paper. A drawing of the test piece is shown in Figure S-3 of supplementary material. One set of specimens had their axis along the build direction, Z; the other set was machined from the XY plane. The strain was measured by a contact extensometer up to 1.2 pct strain, and the elongation was measured after fracture. Heating occurred under conditions of free expansion to reach the test temperatures using a heating rate of 15 °C min^{-1}, and specimens were held at temperature for 20 mins. Specimens were strained at a rate of 8×10^{-5} s^{-1} to 1.2 pct and 8×10^{-4} s^{-1} thereafter (crosshead axial displacement).

2. *Creep testing*

Creep tests were performed on a TOSHIN RT30 30 kN machine. Specimens had a length of 46 mm, a gauge length of 15 mm, and a diameter of 3 mm . A diagram of the test pieces is included in the supplementary material, Figure S-3. The gauge length was finished by grinding to an RA 0.8 using 240 grit SiC paper. Strain was evaluated using an extensometer attached to knife edges, and the temperature was measured with R-type thermocouples attached at three positions in the gauge length. The heating rate prior to the test was 15 °C s^{-1} and the specimen was held at the test temperature for 2 hour prior to testing. Test pieces were oriented either in the build direction (Z) or perpendicular to the build direction (XY). Creep tests were performed at two conditions: 982 °C and 179 MPa and 950 °C and 137 MPa. The latter results are reported in the supplementary material, Figure S-14.

III. RESULTS

A. *Texture and Grain Size Evolution*

The microstructures of the as-built and heat-treated samples were investigated using EBSD, as shown in Figure 1. In the as-built condition, Figure 1(a), the sample exhibits an elongated grain structure with a strong wire texture with the [001] direction parallel to the build direction (BD) or Z-axis, consistent with previous work on CM247LC manufactured by L-PBF.[18,19] This is retained following a 2-hour solution anneal at 1220 °C, Figure 1(b). However, following solution treatment at 1250 °C, Figure 1(c), and HIP at 1250 °C, Figure 1(d), recrystallization had taken place accompanied by significant grain growth. Localized intensity maxima in the pole figures are a result of the limited areas contributing to the pole figure. A full range of orientations is produced by recrystallization and no discernible texture was found following anneal/HIP at 1250 °C. A KAM map of Figures 1(a) through (c) is given in additional material Figure S-4, and shows some very limited recovery and recrystallization in the 1220 °C sample. The fully recrystallized structure consists of elongated grains some 200 μm in diameter and up to 1 mm in length. The average aspect ratio of the larger grains is 5:1. The microstructure closely resembles that reported in the literature for CM247LC after furnace solution treatment for 2 hour at 1250 °C to 1260 °C or for HIP at 1260 °C.[19] Subsequent lower temperature aging at 1080 °C or 870 °C had no detectable effect on the grain structure.

B. *Microstructural Characterization Following HIP and Post-HIP Aging*

1. *Carbides*

Examination of the as-built microstructure in the SEM, Figure 2, revealed MC carbides together with some very fine γ', located between the cellular dendrites. This is consistent with previous detailed work on this alloy[19,20] demonstrating the presence of MC carbides and γ' where the dendrites meet. The cellular dendrites are elongated in the build direction and have a diameter of 0.7 μm. Some of these cellular boundaries are also grain boundaries in the as-built condition.

Recrystallization causes growth of elongated grains up to 200 μm in diameter and is accompanied by substantial coarsening of the carbides, some of which become located within the grains. EDX analysis of these carbides is presented in Figure 3, and shows them to be rich in Hf, Ta, W, and C, as expected for MC carbides.[18,19] One precipitate in the HIP + 1080 °C/4 h + 870 °C/10 h sample in the bottom row of Figure 3 has a W-rich composition containing some Ta and C. This is consistent with the MC carbides identified by Hu[13] in a Hf-free modified CM247LC alloy but is more likely to be an M_6C type carbide because of the lower C content indicated in Figure 3 and the close proximity of other MC carbides of a very different composition. Chromium-rich $M_{23}C_6$ carbides were also identified at the grain boundaries in this heat-treated sample and are shown in supplementary material Figure S-5.

X-ray diffraction spectra from the same three samples, HIP, HIP + 1080 °C/4 h, and HIP + 1080 °C/4 h + 870 °C/10 h (Figure S-6 in supplementary material), showed the presence of the γ, γ' phases and MC carbides as expected. No change was seen with heat treatment. No other carbide phases were present in

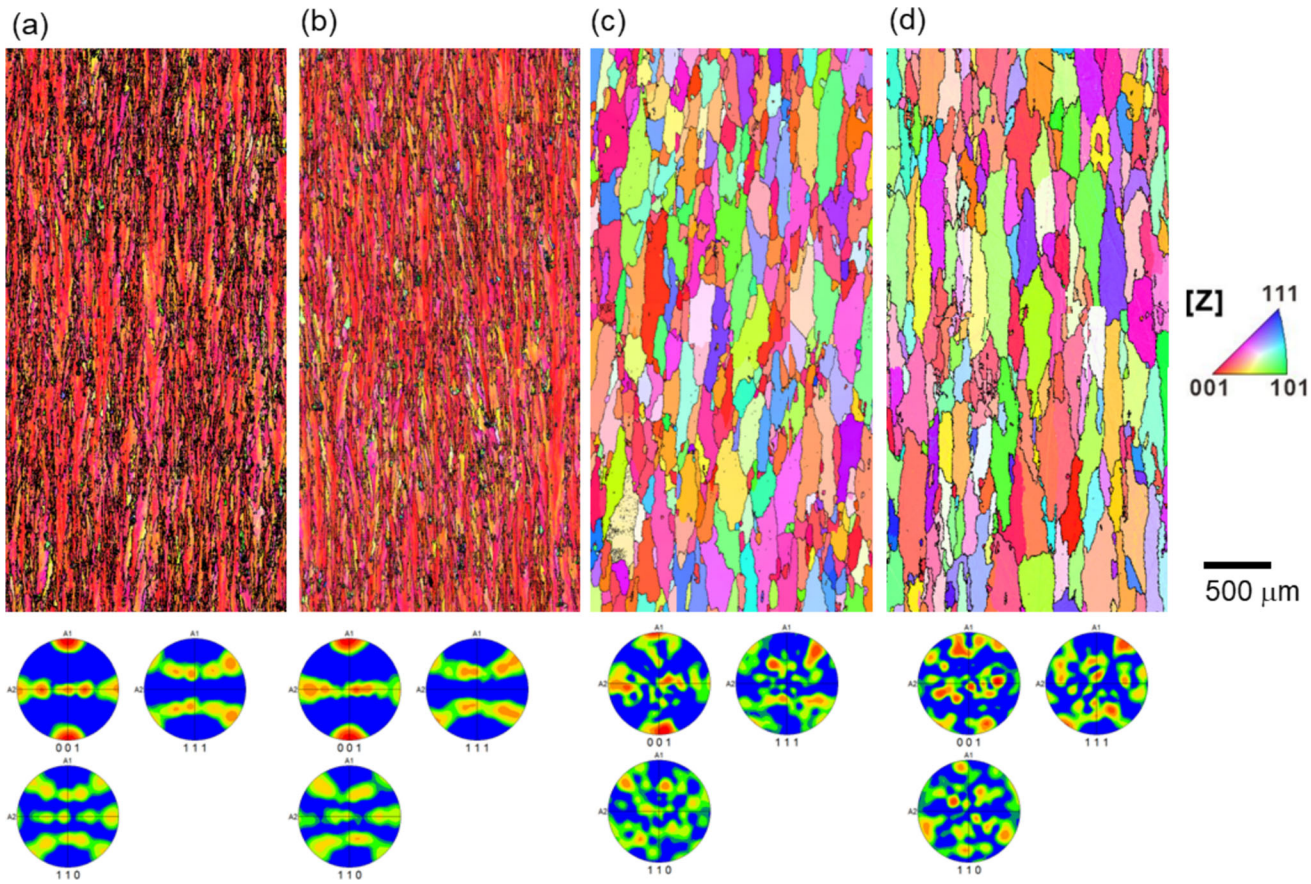

Fig. 1—SEM-EBSD and corresponding inverse pole figures of (*a*) as-built, and heat treated at (*b*) 1220 °C/2 h, (*c*)1250 °C/2 h and (*d*) HIP 1250 °C/100 MPa/2 h. Samples cut parallel to the build direction, which is vertical in the images. Colors correspond to the orientation in the build (Z) direction (Color figure online).

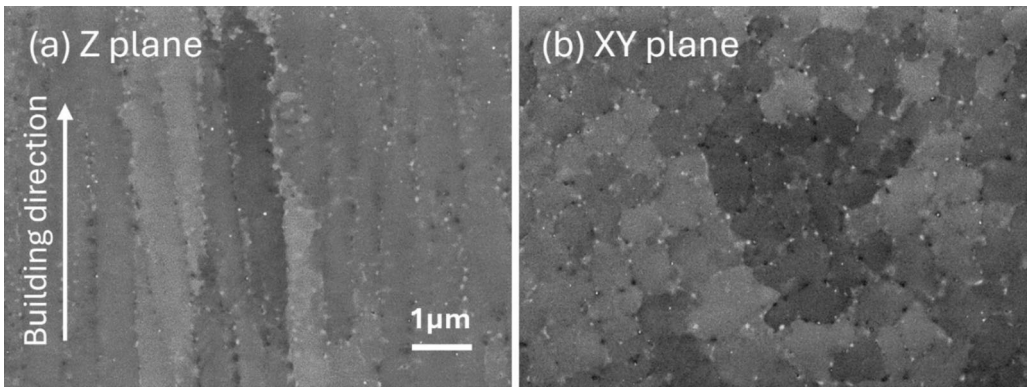

Fig. 2—Secondary electron (SE) SEM images of etched as-built samples showing the grain structure and the carbides (bright contrast) located largely at the grain boundaries. (*a*) Longitudinal section, build direction vertical; (*b*) Transverse section.

sufficient quantity to form distinct peaks, and it was not possible to resolve the γ and γ' phases as their lattice parameters are so similar.

2. *γ' morphology*

Secondary electron (SE) SEM images of etched samples are shown in Figure 4, which reveal the γ/γ' features of the full range of those heat treatments that include a HIP treatment at 1250 °C following the build. Table II gives measurements of size and volume fraction of γ' derived from each sample.

The γ' morphology following high-temperature solution anneals at 1220 °C and 1250 °C without the HIP is shown in Figures 5(a) and (b), respectively. The 1220 °C solution heat treatment is insufficient to fully dissolve the γ' from the as-built structure and hence larger irregular γ' forms from the undissolved γ', together with some coarse secondary γ' between, Figure 5(a). The

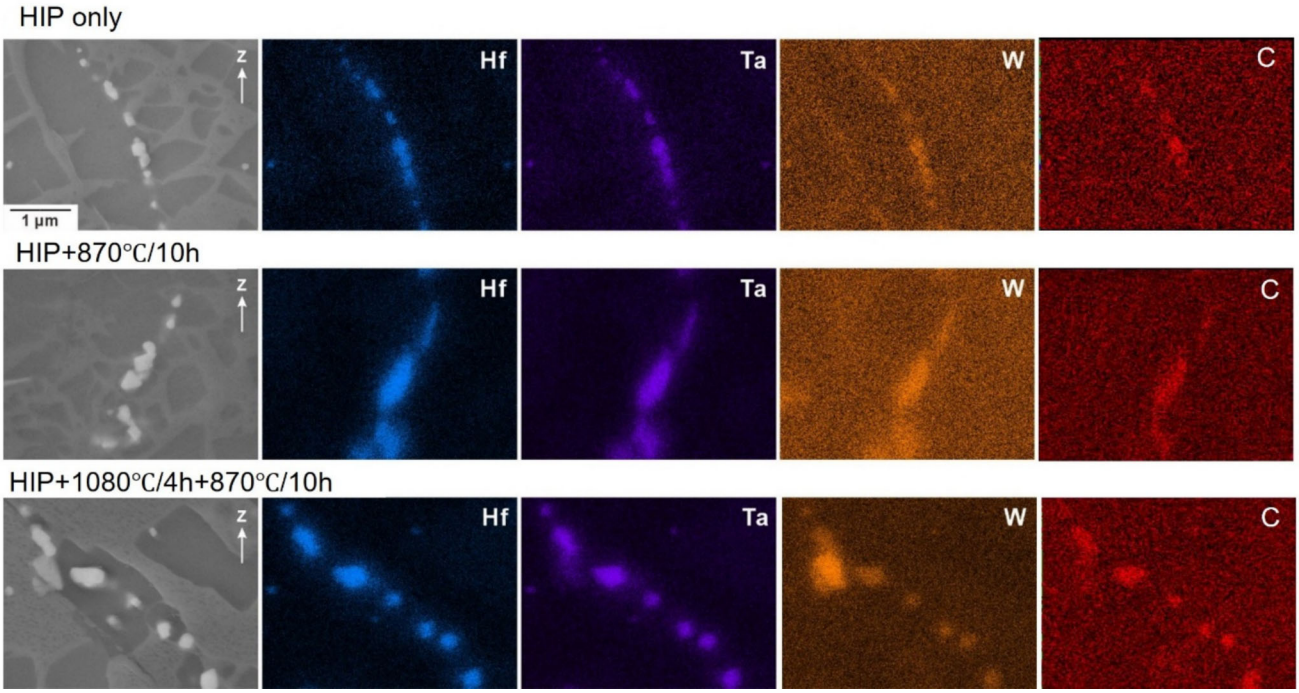

Fig. 3—EPMA analysis of carbides in samples with various heat treatments following HIP.

1250 °C solution anneal gives a microstructure of fine well-aligned primary precipitates of average size 0.48 μm, Figure 5(b). This is expected from a full dissolution of the γ' followed by a rapid cool executed and is similar to the γ' observed by several researchers.[17,21,22] It is in stark contrast to the primary structures resulting from the HIP and slow cool, where the primary γ' precipitates are around 2 μm in diameter and exhibit the octahedral subdivision more characteristic of lower volume fraction polycrystalline superalloys identified by Ricks *et al.*[23] This is a result of the much slower cooling rate occurring after the HIP anneal, which is essentially a furnace cool rather than an air quench.[24]

The HIP treatment and subsequent slow cool determines the structure of the primary γ' precipitates for all these heat treatments. Table II gives the sizes and volume fractions of the γ and γ' in each sample. Figure S-7 in supplementary material shows examples of the images used to produce Table II. Looking at Figure 4, it is apparent that the number and spacing of the larger primary precipitates remain largely unchanged by the heat treatments following the HIP. However, the 1080 °C heat treatment has the effect of reducing the volume fraction of primary γ' as the time at temperature increases from 0 to 2 to 4 hours. This is evident looking down each of the columns where the length of the1080 °C anneal is increasing, each column having the same subsequent heat treatment at 870 °C. The volume fraction is reduced by the shrinkage of individual precipitates and the loss of the smallest. This has the effect of reducing the volume fraction of primary γ' while increasing the average size and reducing the precipitate density as seen in Table II. Thus, for the left-hand column of Figure 4, the volume fraction of primary γ' decreases from 70.4 to 69.2 to 61.0 pct as the anneal at 1080 °C increases from 0 to 2 to 4 hour, but the average γ' diameter increases from 827 to 917 to 951 nm, and the precipitate density decreases.

We now look at the effect of the lower temperature anneal at 870 °C. Along each row of Figure 4, the 870 °C anneal increases from 0 to 10 to 15 hour, left to right. For the top row without a heat treatment at 1080 °C, the volume fraction of primary γ' increases from 70.4 to 75.8 to 77.6 pct as the secondary γ' is absorbed. However, for the middle and lower rows, having had heat treatments at 1080 °C for 2 and 4 hour, respectively, the primary γ' tends to be quite stable or fall, but the fine secondary γ' precipitated during the rapid cool from 1080 °C coarsens. The as-HIPed sample, top left, shows a few coarse secondaries which dissolve during the 1080 °C anneal. No secondary γ' is seen in the left-hand column, middle and bottom, as it is too fine to be resolved in the SEM at this magnification, but γ' has been detected in the TEM as will be discussed later. In the middle and right-hand columns, heat treated for 10 and 15 hours at 870 °C, respectively, the secondary γ' coarsens progressively.

C. *Mechanical Data*

1. *Tensile behavior*

Tensile test data measured at 25 °C and 900 °C are given in Table III. The room-temperature proof stress of the as-built structures are rather lower than the fine-grained conventionally cast material tested by Huang,[25] but the UTS and ductility are both higher. At 900 °C, Table III compares HIPed samples, having

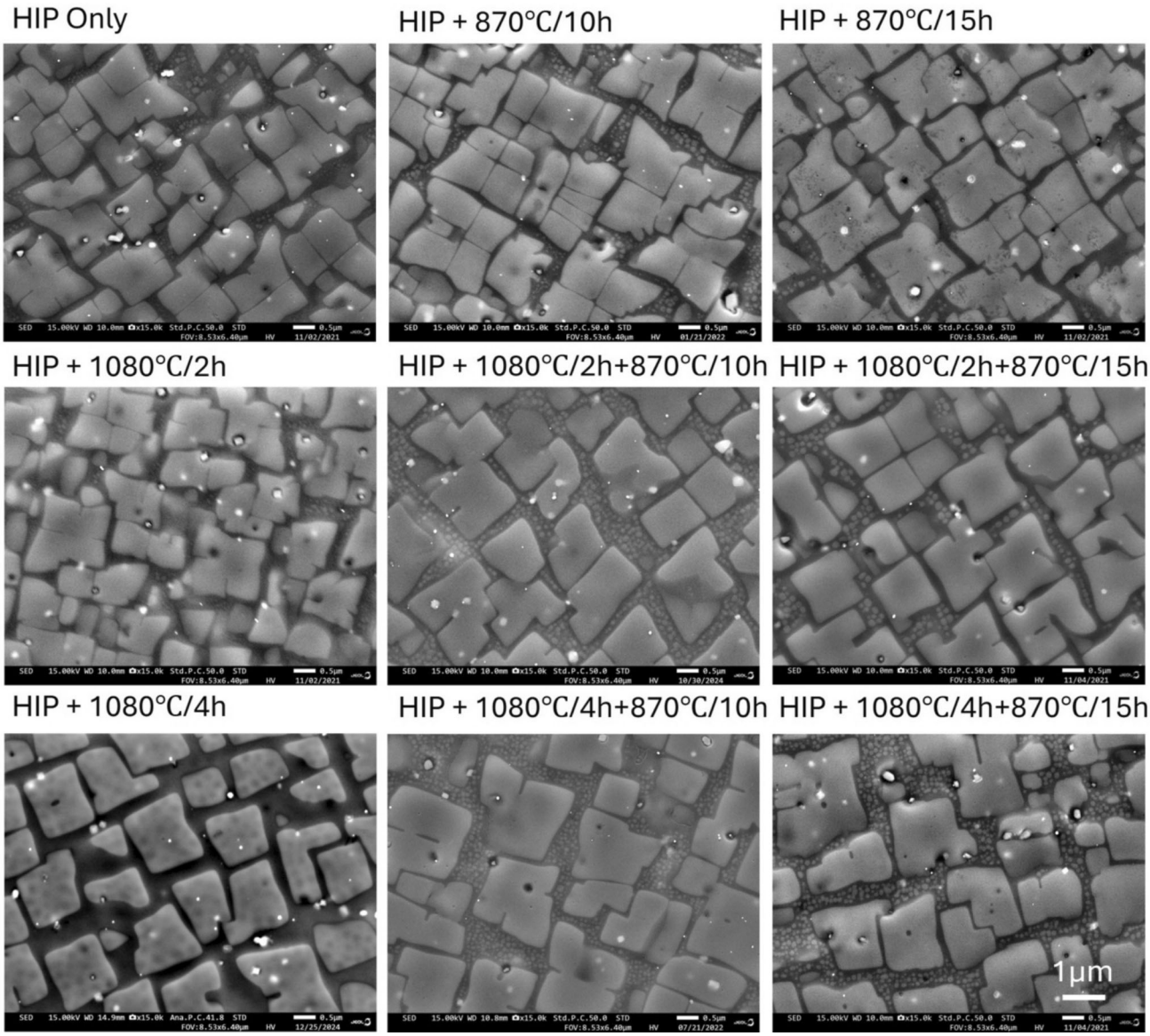

Fig. 4—Images (SEM) showing the primary and secondary γ' morphology for selected heat treatments following a HIP treatment.

various heat treatments, with those given a 2-hour solution treatment at 1220 °C and 1250 °C followed by two-step aging of 1080 °C for 4 hour + 870 °C for 20 hour. Tensile curves up to 1.2pct strain for the HIPed samples are given in supplementary material, Figure S-8.

The proof strength varies greatly with heat treatment, with the highest value (~640 MPa) for the HIP + 4 h/1080 °C + 10 h/870 °C, and the lowest values (~520 MPa) for the non-HIPed samples and those without an anneal at 1080 ºC. Comparing proof stresses in the Z and XY orientations shows similar results, with either value almost equally likely to exceed the other. The variability averages about 2 pct of the proof stress, with a maximum value of 5 pct. The UTS is remarkably consistent at around 800 MPa, peaking for the heat treatment with the highest proof stress and showing very small variation between the Z and XY orientations. One sample failed at 0.3 pct strain and 662 MPa (HIP + 4 h/870 °C, XY) before it reached peak strength, probably due to a large defect in the sample. Although the proof strength and UTS change little with orientation, there is significant anisotropy in the ductility, with the Z direction showing very good ductility and the transverse XY ductility rarely exceeding 5 pct.

There is a significant increase in proof stress following the anneal at 1080 °C, with 4 hours being more effective than 2. Without the anneal at 1080 °C, none of the samples exceeds a proof stress of 550 MPa. Following HIP + 1080 °C/4 h, the proof stress improves slightly with an anneal of 10 hour at 870 °C, from 635 to 640 MPa, but decreases sharply on a longer anneal of 15 hour to 540 MPa. This pattern is replicated in the samples with a 2-hour heat treatment at 1080 °C, with the proof stress dropping from 606 to 541 MPa. Both

Table II. Quantification of Primary and Secondary γ' for Various Heat Treatments of L-PBF Fabricated CM247LC

Heat Treatment				Primary γ'				Secondary γ'			Matrix
Solution Treatment, 2 h		Sub-Solvus 1080 °C	Aging 870 °C	Area Fraction	Average Size	Average Length	Density	Area Fraction	Ratio in Matrix	Average Area	Average Diameter	Area Fraction
°C	MPa	h	h	pct	μm^2	μm	$/\mu m^2$	pct	pct	$\mu m^2 \times 10^3$	nm	pct
1220		4	20	62.2	1.069	0.909	0.58	5.4	14.3	8.82	102.1	32.4
1250		4	20	74.7	0.250	0.447	2.98	—				25.3
1250	100			70.4	0.887	0.827	0.79	1.4	4.6	3.62	63.0	28.2
1250	100		10	75.8	0.888	0.846	0.85	2.8	11.7	5.31	77.2	21.4
1250	100		15	77.6	1.802	1.173	0.43	0.5	2.4	6.73	90.1	21.9
1250	100	2		69.2	1.105	0.917	0.63	—				< 30.8
1250	100	4		61.0	1.055	0.951	0.58	—				< 39.0
1250	100	2	10	67.8	1.976	1.269	0.34	7.1	22.1	8.89	102.6	25.1
1250	100	2	15	65.4	1.252	1.007	0.52	5.2	14.9	13.86	128.2	29.4
1250	100	4	10	60.5	1.040	0.947	0.52	7.4	18.7	4.72	75.6	32.1
1250	100	4	15	63.0	1.351	1.072	0.47	8.8	23.7	6.95	91.7	28.2

γ' area measured from images and γ' diameter is equivalent circle diameter. Mean values calculated from each data set.

the solution heat-treated samples without the HIP show low proof stresses, with the solution treatment at 1250 °C having the lowest proof stress measured of 515 MPa. It should be noted that both these samples had an anneal of 20 hour at 870 °C.

2. *Temperature dependence*

Further tensile tests were conducted from 700 to 1000 °C on two heat treatment conditions to investigate the improved performance from the double heat treatment (A), sample 5 in Table III, (HIP + 1080 °C/4 h + 870 °C/10) compared to the single stage heat treatment (B), sample 3 in Table III, (HIP + 870 °C/15 h). Figure 6 shows the proof stress, UTS, and elongation data for tests in Z and XY directions. The data from this figure are given in Table S-1 of supplementary material. Tests show a maximum in the proof stress at around 800 °C and a consistent advantage of the double heat treatment, A. The isotropy of the proof stress and UTS throughout the temperature range is striking, but there is a significant effect of orientation on ductility, with the transverse XY samples showing consistently reduced elongation, Figure 6(b). For most samples, elongation to failure drops with test temperature.

3. *TEM of deformation structure*

Differences in tensile behavior can be ascribed to different primary and secondary γ' distributions and resultant dislocation–particle interactions. To investigate this further, tensile test samples interrupted at 0.2 pct strain in the Z direction were examined in the TEM. The deformation structure of the samples deformed at 900 °C to 0.2 pct strain and having HIP plus 4 hour at 1080 °C followed by 0, 10, and 15 hour at 870 °C are shown in Figures 7(a) through (c), respectively. Figure 7(d) shows the sample having a HIP + 870 °C/15 h, omitting the 1080 °C anneal.

In all cases, there is very little dislocation activity in the primary γ' precipitates; deformation at this temperature essentially occurs in the γ matrix. With no anneal at 870 °C, Figure 7(a), no secondary precipitates are visible and the dislocations in the γ are held up at the interface with the primary γ' precipitates. Further imaging of this area using a dark field superlattice diffraction spot shows evidence of precipitates, the largest of which are about 25 nm in diameter and indicated by white arrows in Figure 8. The sharper brighter spots correspond to the contrast from emergent dislocations imaged in bright field and are indicated by blue arrows. Full sets of images for each heat treatment allow comparison with dislocations and are given in supplementary material, Figures S-9 to S-13.

After 10 hour at 870 °C, Figure 7(b), secondary γ' precipitates are visible and are interacting with the dislocations in the γ phase resulting in some dislocations within the γ phase and some at the interface with the primary γ'. After 15 hour at 870 °C, the dislocation density in the γ has much increased and there is clear evidence of dislocations looping around and between the coarser secondary γ'. In the final micrograph, Figure 7(d), from a single stage heat treatment of

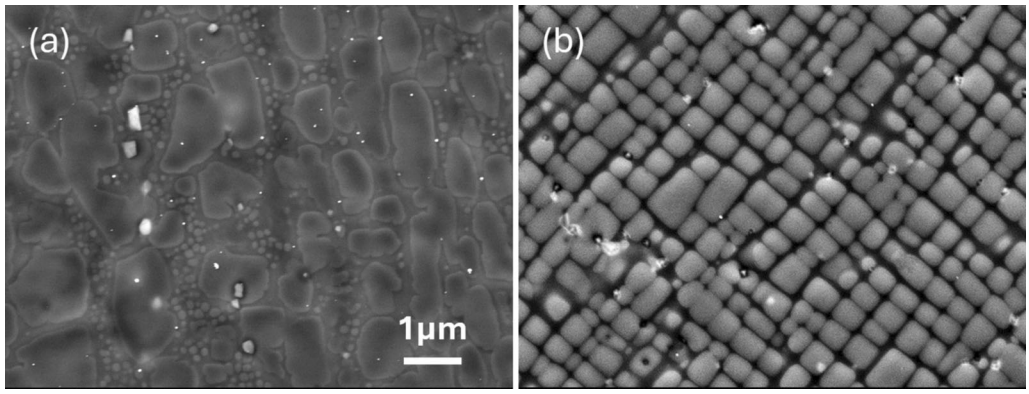

Fig. 5—Non-HIPed material: Morphology of γ' following anneal at (*a*) 1220 °C and (*b*) 1250 °C, both followed by 1080 °C/4 h and 870 °C/20 h.

15 hour at 870 °C following HIP, the primary γ' phase has a high-volume fraction leaving relatively little room for dislocation motion in between. Within the γ, the secondary precipitates are relatively sparse and large and dislocations mobile in the γ are looping around them, creating dislocation networks as in Figure 7(c). Without the heat treatment at 1080 °C, Figure 7(d), the increased volume fraction of primary γ' is clear.

4. *Creep behavior*

Creep results at 982 °C and 179 MPa are listed in Table IV. The HIP treatment gives a significant improvement in creep life in both orientations. Ductility and life to failure are both very poor for samples tested in the XY orientation, at right angles to the elongated grains in the build direction. Among the samples tested in the Z direction, the marginally best performance is achieved with two-stage aging, but all the HIPed specimens achieve a good creep life close to the 143 hour from the as-cast specimen, at a fraction of the ductility. As the test temperature is well in excess of 870 °C, secondary annealing time is largely irrelevant, reflected in the very similar performance of samples (d) and (e) in Figure 9.

The creep curves (b through e) on Figure 9 are fundamentally very similar but the transition to tertiary creep for the two samples which were not HIPed [Figures 9(a) and (b)] is very much more rapid. This can be attributed to the presence of porosity, albeit at a low level, in the as-built material resulting in the formation of cracks in the early stages of creep. The non-HIPed sample, Figure 9(a), solutioned at 1220 °C shows the worst creep performance and the absence of a full solution anneal and full recrystallization gives a very significant increase in the primary creep strain and a much-reduced creep life. The two samples with a HIP plus single aging treatment at 870 °C [Figure 9(c)] and 1080 °C [Figure 9(d)] are almost identical to 80 pct life.

The most interesting comparison is between the furnace treated sample solution treated at 1250 °C with a two-stage heat treatment at 1080 °C/4 h and 870 °C/20 h, Figure 9(b), and the best performing sample with a HIP and two stage heat treatment of 1080 °C/4 h and 870 °C/10 h, Figure 9(e). The HIPed sample Figure 9(e) has the longest life but initially the more rapid creep rate. However, the un-HIPed sample Figure 9(b) with the more conventional fine cubed γ' morphology, Figure 5(b), has the lowest initial creep rate and the smallest amount of primary creep strain. The minimum creep rates of these two tests are very similar at about 4×10^{-8} s^{-1}, but the primary creep strain in the HIPed sample is about 0.15 pct, 10 times larger than the solution treated sample, 0.015 pct. The HIP treatment, however, does lead to more than double the life to rupture and a fourfold increase in ductility.

Samples of two HIPed and heat-treated conditions: HIP + 870 °C/15 h and HIP + 1080 °C/4 h + 870 °C/10 h, were tested at the standardized creep conditions of 950 °C and 137 MPa. For both samples in the Z orientation, the creep life exceeded 1300 hour reaching over 1500 hour for the two-stage heat treatment. Details are given in supplementary material, Figure S-14.

The progressive formation of voids on the grain boundaries in the later stages of creep increases the creep strain. In the case of the XY samples the higher density and length of boundaries at right angles to the stress axis compared to the Z samples results in not only increases measured creep strain but leads to earlier failure, Figure 10. Optical micrographs of the same area showing a wider view are included in supplementary material Figure S-15.

IV. DISCUSSION

A. *Microstructure*

When used as an AM alloy with these optimized energy input parameters L-PBF CM247LC gives a crack-free structure with a strong [001] wire texture and an almost random spread of the secondary orientations as shown in Figure 1(a) and the associated pole figures. The sample solution treated at 1220 °C remains almost completely unrecrystallized, Figure 1(b), indicating that 1220 °C is well below the γ' solvus. The heat treatments at 1250 °C in both the solution treated and HIPed samples, Figures 1(c, d), completely recrystallize the as-built material, causing significant grain growth and removing the wire texture. The granular nature of the inverse pole figures in Figures 1(c, d) is a result of the

Table III. Tensile Properties After Various Heat Treatments

Heat Treatment	Build Direction	Temp °C	0.2 pctPS MPa	UTS MPa	El Pct	RA Pct
As-Built	Z	Room T	910	1393	21.1	20.9
	XY	Room T	927	1409	22.4	24.1
1220 °C/2 h + 1080 °C/4 h + 870 °C/20 h	Z	900	544	817	16.1	20.9
1250 °C/2 h + 1080 °C/4h + 870 °C/20 h	Z	900	515	759	10.1	17.4
HIP + 870 °C/10 h	Z	900	545	798	20.0	21.4
HIP + 870 °C/15 h	Z	900	527	793	19.1	19.5
HIP + 1080 °C/2 h + 870 °C/10 h	Z	900	606	822	9.7	20.2
HIP + 1080 °C/2 h + 870 °C/15 h	Z	900	541	794	10.2	18.5
HIP + 1080 °C/4 h	Z	900	635	802	12.1	14.6
HIP + 1080 °C/4 h + 870 °C/10 h	Z	900	640	846	13.1	21.6
HIP + 1080 °C/4 h + 870 °C/15 h	Z	900	540	796	17.2	20.6
1220 °C/2 h + 1080 °C/4 h + 870 °C/20 h	XY	900	528	758	0.6	1.8
1250 °C/2 h + 1080 °C/4h + 870 °C/20 h	XY	900	527	785	4.2	3.6
HIP + 870 °C/10 h	XY	900	533	766	5.3	5.6
HIP + 870 °C/15 h	XY	900	517	771	7.1	8.4
HIP + 1080 °C/2 h + 870 °C/10 h	XY	900	608	816	4.7	5.3
HIP + 1080 °C/2 h + 870 °C/15 h	XY	900	552	788	5.6	5.6
HIP + 1080 °C/4 h	XY	900	645	662	0.3	0.9
HIP + 1080 °C/4 h + 870 °C/10 h	XY	900	634	828	3.8	5.8
HIP + 1080 °C/4 h + 870 °C/15 h	XY	900	571	802	3.8	8.3

limited area from which these were obtained rather than any residual texture. Markanday *et al.*[11] report partial recrystallization of CM247LC after a HIP at 1250 °C and complete recrystallization after a further anneal at 1260 °C. This slightly higher temperature can be attributed to the sensitivity of the γ' solvus, controlling the recrystallization, to small changes in composition within the alloy specification. The resulting grain structure, elongated in the build direction, largely resembles a DS microstructure but with many more boundaries perpendicular to the build direction (Z) which we discuss later.

Carbides are initially deposited between the cellular dendrites during solidification, Figure 2, and coarsen to about 100 nm after the HIP, often located mid-grain as seen in the bright precipitates in Figure 3. Chains of slightly larger MC carbides, up to about 500 nm, are located at grain boundaries and are imaged in Figure 3. The structure of the carbides is consistent with the MC crystal structure as examined by X-ray diffraction scans of the HIPed, HIPed + 1080 °C/4 h, and HIPed + 1080 °C/4 h + 870 °C/10 h samples shown in Figure S-6 of supplementary material. The structure and morphology remain unchanged with heat treatments following the HIP, as does the composition, Figure 3. Carbides are rich in W, Hf and to a lesser extent Ta, all strong MC carbide formers. These observations are broadly in line with those of Markandy[11] who note the presence of MC carbides in as-built CM247LC and the coarsening of these carbides during the HIP treatment. Occasional precipitates richer in W were observed, but not identified, as were chromium-rich carbides in the boundaries.

Although recrystallization is not affected by the substitution of the HIP, Figures 4 and 5 show that the HIP at 1250 °C is not equivalent to a solution heat treatment at the same temperature. As demonstrated by the work of Martelli,[12] this is not due to the pressure but the difference in cooling rate where forced cooling is not available in the HIP equipment. The slow cool from the HIP treatment (13.3 K min^{-1}) results in very large octahedrally dissected γ' up to 5 μm in diameter in all the HIPed samples, Figure 4. During cooling, the volume fraction of γ' tracks the equilibrium value. In contrast, the rapid cool from the solution treatment at 1250 °C (312 K min^{-1}), gives the conventional single crystal microstructure of closely aligned cubic precipitates about 0.5 μm in size, Figure 5(b), since nucleation occurs at lower undercooling.

The anneal at 1080 °C for 0, 2 and 4 hours, Figure 4, shows a progressive shrinkage of the primary γ' volume fraction. The anneal at 1080 °C also dissolves the coarse secondary precipitates formed between the primaries, partially after 2 hour and fully after 4 hour. On cooling, the γ is filled with fine secondary γ' precipitates forming during the rapid cool from 1080 °C. The 870 °C anneal has no further effect on the primary γ' but does coarsen the fine secondary γ' located in the γ channels. In the samples without a 1080 °C anneal (top row of Figure 4), the secondaries already present are coarse and sparse, having been formed during the slow cool from the HIP. These will absorb the excess γ-forming elements during the slow cool, and the heat treatment at 870 °C has little further coarsening effect. In the samples heat treated for 4 hour at 1080 °C, (Figure 3, third row) the 870 °C heat treatment has the most effect, progressively growing the fine γ' precipitates formed during the cool from 1080 °C to give an even distribution of fine γ' in the roughly 40 pct of γ located between the large primary γ' precipitates. The equilibrium value of γ' at 1080 °C is around 43 pct calculated from Thermocalc by Griffiths *et al.*[22] The heat treatments at 1080 °C and 870 °C have apparently little effect on the carbides as shown in Figure 3.

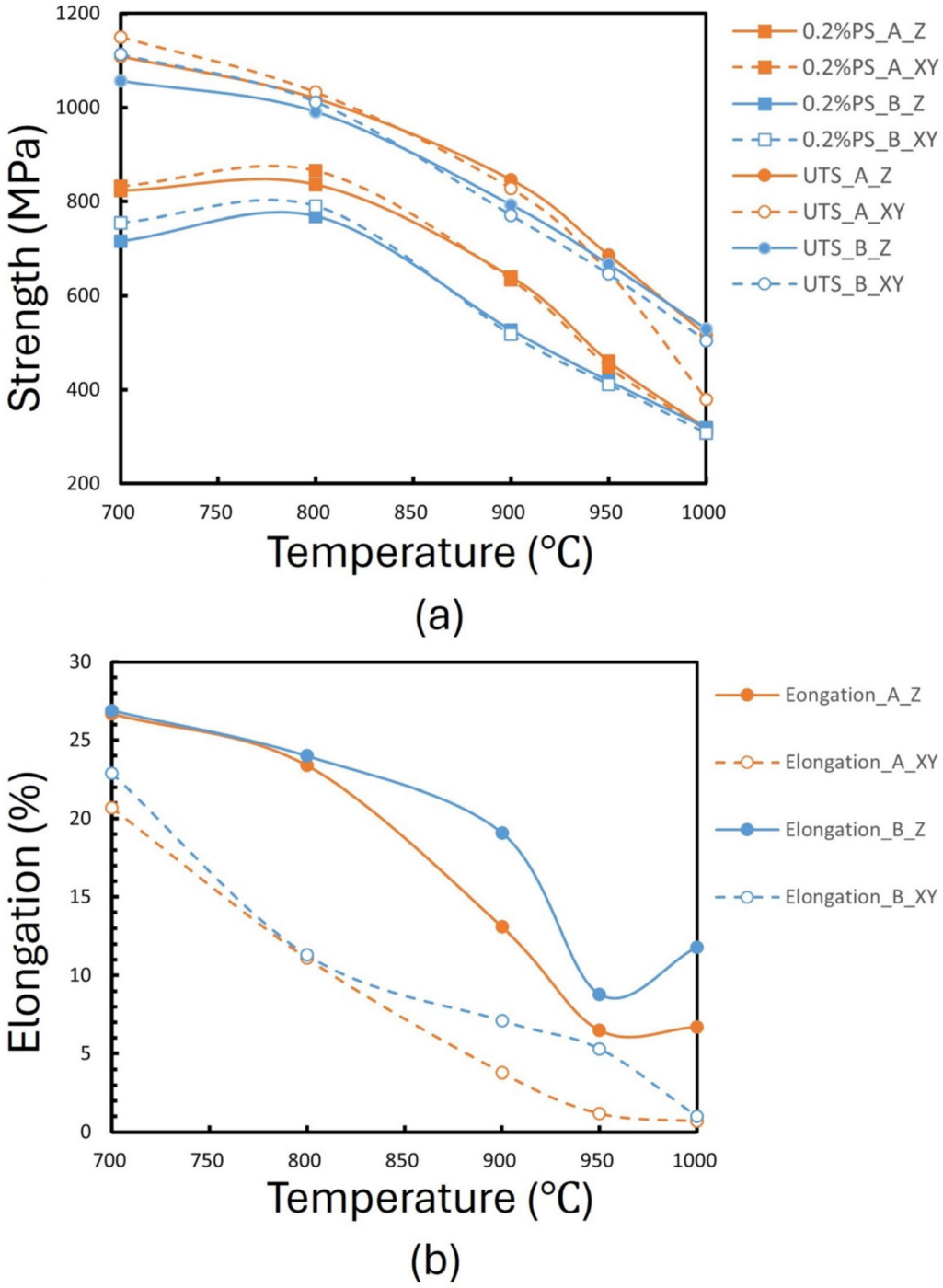

Fig. 6—(*a*) 0.2 pct Proof stress and UTS as a function of temperature and (*b*) elongation at failure. Two heat treatments are tested, A: HIP + 1080 °C/4 h + 870 °C/10 (in orange) and B: HIP + 870 °C/15 h (in blue) and samples are cut parallel to the build direction Z and perpendicular to XY (Color figure online).

In these HIPed alloys, the two anneals at 1080 °C and 870 °C, borrowed from the heat treatment of alloys fast cooled from a full solid solution anneal, have very different functions from those in conventional furnace treatments. The latter are formulated on the assumption of a distribution of relatively fine regular γ' formed on rapid cooling from a fully single-phase structure. The 1080 °C anneal optimizes the size of those primary precipitates and allows them to align fully to minimize the elastic energy of the microstructure generated by the misfit stresses. The anneal at 870 °C clears the secondary precipitates from the narrow γ channels thus reducing primary creep[26,27] and increasing creep rupture life. However, in the HIPed samples with very coarse primary γ', the 1080 °C heat treatment essentially dissolves the smaller primary γ' between the over-sized

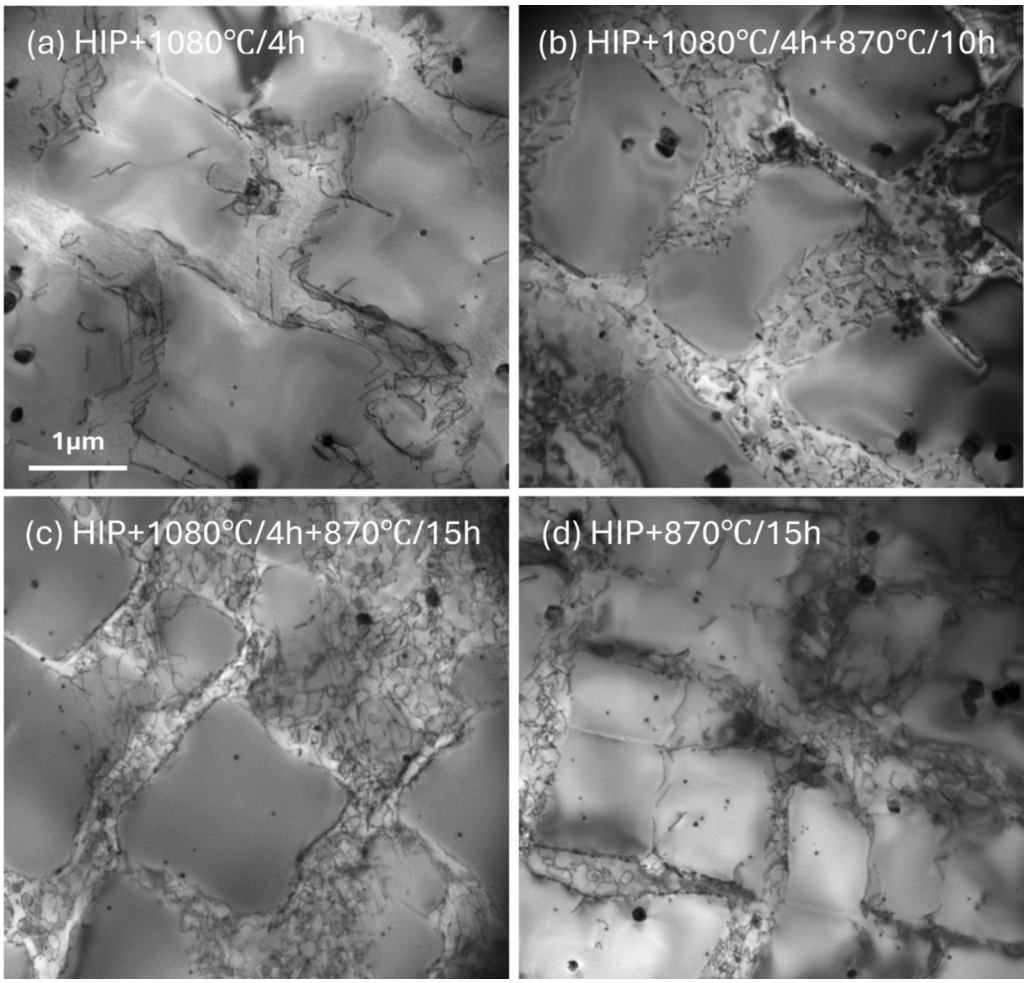

Fig. 7—TEM micrographs of the dislocation structure following deformation at 900 °C to 0.2 pct strain. (*a*) HIP + 1080 °C/4 h, (*b*) HIP + 1080 °C/4 h + 870 °C/10 h, (*c*) HIP + 1080 °C/4 h + 870 °C/15 h, (*d*) HIP + 870 °C/15 h. All taken in two-beam conditions of the type [200]. Further micrographs of each sample, including dark field and diffraction conditions, are included in supplementary material Figures S-9 to S-13.

primary precipitates and progressively establishes the equilibrium γ' volume fraction at 1080 °C. The 870 °C heat treatment ages the fine secondary precipitates formed during the cool from 1080 °C. We now turn to the effect of this on the mechanical properties.

B. *Tensile Properties*

The proof stress is sensitive to the γ/γ' microstructure, Table III. The best performance is shown by the HIP + 1080 °C/4 h + 870 °C/10 h heat treatment, (640 MPa) but is only slightly above the HIP + 1080 °C/4 h (635 MPa) and within the error range. The sample with the longer anneal at 870 °C of 15 hour shows a drop in proof stress of nearly 100 MPa. The effect of the additional aging at 870 °C is mirrored in the specimens annealed for 2 hour at 1080 °C, but with reduced values.

With respect to the HIP + 1080 °C/4 h samples with 0, 10 and 15 hour heat treatments at 870 °C, the bottom row of Figure 4, we suggest the proof stress is following the age hardening of the secondary precipitates in the γ. The small secondaries are underaged in the as-cooled condition at about 25 nm (proof stress 635 MPa), but after 10 hour, just exceed the peak-aged condition at 75 nm. After 15 hour at 870 °C, the precipitates are overaged (92 nm) and the proof stress drops. This is consistent with the observations of Griffiths *et al.* in the same L-PBF alloy.[22] These authors note, from hardness data, the peak-aging time at 850 °C to be 8 hour and measure a precipitate size of 50 nm. The values for 10 and 15 hour given in Table II, are both measured from the SEM images in the etched condition, Table II. However, examination of the superlattice dark field pictures of these two heat treatments given in supplementary material indicates a smaller size of around 60 nm in the 10 hour heat treatment. Many of the smaller precipitates would have been lost in the etching used to assess γ' size in the SEM, thus increasing the measured average. Examination of the size after 15 hour exposure at 870 °C of 92 nm is consistent with the TEM observations.

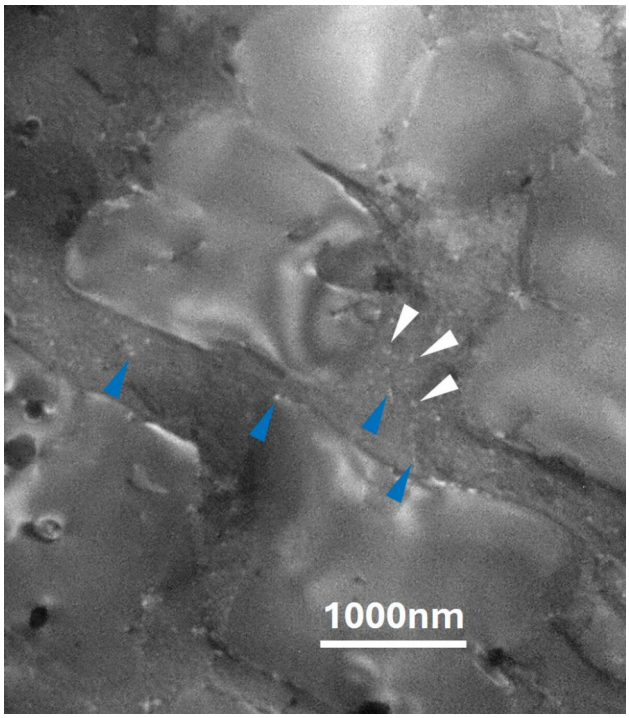

Fig. 8—Superlattice [100] dark field of single stage HT 1080 °C for 4 h. Examples of precipitates are indicated by white arrows and contrast from emergent dislocations by blue arrows (Color figure online).

The TEM micrographs Figure 7 confirm that there is essentially no dislocation activity in the γ' precipitates. Thus, the proof stress at 900 °C is determined principally by dislocation activity in the γ phase and particularly, by the size of the secondary precipitates. The proof stress also shows a steady improvement with the longer anneal at 1080 °C from 0 to 2 hour and then 4 hour, at 545, 606, and 640 MPa, respectively, all with HIP and the subsequent 870 °C/10 h anneal. This suggests that the decrease in the volume fraction of γ' primary phase is also beneficial for the proof stress by increasing the volume of γ plus fine secondary γ'. However, optimizing the proof stress may be at the expense of the ductility.[28]

A peak-aging time of between 0 and 10 hour at 870 °C, is consistent with the TEM observations in Figure 7. A high dislocation density, including loops, is clearly visible in the gamma channels of the 10 and 15 hour samples Figures 7(b) and (c). This suggests dislocations are bypassing the secondary precipitates. However, very few are seen in the γ' of the single stage heat treatment where the underaged precipitates are cut, leaving no dislocation loops and just pile-ups at the primary γ' precipitates, Figure 7(a). The heat treatment HIP + 870 °C/10 h, Figure 7(d), will not benefit from fine precipitates in the γ because it has not been fast cooled from 1080 °C, hence the low proof stress of 545 MPa.

Trends in ductility are hard to discern as the results come from a single test at each heat treatment. For tests receiving a HIP and annealed at 1080 °C for 4 hour, the effect of secondary γ' size after 0, 10, and 15 hour at 870 °C on the ductility is a slight increase from 12.1 to 13.1 and 17.2 pct, respectively. The effect of the primary γ' size can be followed from tests receiving a HIP, annealed for 0, 2, and 4 hour at 1080 °C and thereafter each receiving 10 hour at 870 °C. Here the ductility after 0, 2 and 4 hour at 1080 °C was 20, 9.7, and 13.1 pct, respectively. There is no strong trend in ductility; arguably there is a slight increase with coarser secondaries but, as ductility is subject to macroscopic features such as gross porosity, a wide variation between tests is expected.

We conclude that a 4-hour anneal at 1080 °C gives optimum volume fraction of the γ and secondary γ' and fully clears all the smaller precipitates between the primaries after the HIP. Thus, the fast cool from 1080 °C gives nanoscale secondaries which are slightly underaged. A further anneal at 870 °C has a slight beneficial effect at 10 hour but overages at 15 hour. The latter two heat treatments are both past the peak in proof stress as they both exhibit looping, and a slightly shorter anneal than the 10 hour at 870 °C used here might give a higher yield stress, potentially at the expense of the ductility.[28]

What is really interesting here is that all the HIPed microstructures give a better proof strength than the more rapidly quenched structure from the 1250 °C anneal. Note the compositions and conventional microstructures used for single crystal and DS alloys are optimized for creep, not tensile properties. The conventional heat treatments are formulated to produce a fine distribution of regular γ' formed on rapid cooling from a fully single-phase structure. The microstructure after HIP and a slow cool is large bisected cubic primary γ' with fairly coarse secondaries formed during the continuous cool, Figure 4, top left. This is very similar to the microstructure observed by Divya *et al.* in L-PBF CM247LC after annealing subsolvus at 1230 °C and an air cool[19] and shows how sensitive the γ/γ' microstructure is not only to the starting microstructure but also to the cooling profile. Coarse primary γ' and fine precipitation hardened γ and γ' in between resemble the microstructures of polycrystalline alloys for disk applications, optimized for tensile and fatigue properties. In this microstructure, following the slow cool from the HIP, the anneal at 1080 °C performs a very different function, in the sense that it is determining the primary γ' volume fraction. So, as a lower primary volume fraction of primary γ' gives better tensile properties, an anneal at a temperature higher than 1080 °C might further improve the proof strength by increasing the volume fraction of fine γ/γ'.

C. *Creep Properties*

Creep tests were run at 982 °C and 179.3 MPa on a reduced subset of the samples tested for tensile properties. These included the best performing heat treatments and the solution heat-treated samples. The results are compared with results from Erickson[10] on CM247LC in cast form in Table IV.

Table IV. Creep Test Data Measured at 179 MPa/982 °C Compared with Results from Directionally Solidified Cast CM247LC, from Erickson[10]

Heat Treatment	Direction	Creep Life h	El Pct	RA Pct
1220 °C/2 h + 1080 °C/4 h + 870 °C/20 h	Z	24.2	1.8	1.7
1250 °C/2 h + 1080 °C/4 h + 870 °C/20 h	Z	57.2	1.9	2.8
HIP + 870 °C/15 h	Z	119.6	12.2	18.3
HIP + 1080 °C/4 h	Z	105.7	8.9	12.3
HIP + 1080 °C/4 h + 870 °C/10 h	Z	127.4	12.5	15.8
1220 °C/2 h + 1080 °C/4 h + 870 °C/20 h	XY	4.6	7.0	9.1
1250 °C/2 h + 1080 °C/4 h + 870 °C/20 h	XY	4.5	1.4	7.9
HIP + 870 °C/15 h	XY	33.6	1.5	4.7
HIP + 1080 °C/4 h	XY	31.7	1.4	2.5
HIP + 1080 °C/4 h + 870 °C/10 h	XY	36.5	1.1	0.7
DS-CM247LC	L	143.3	38.7	53.9

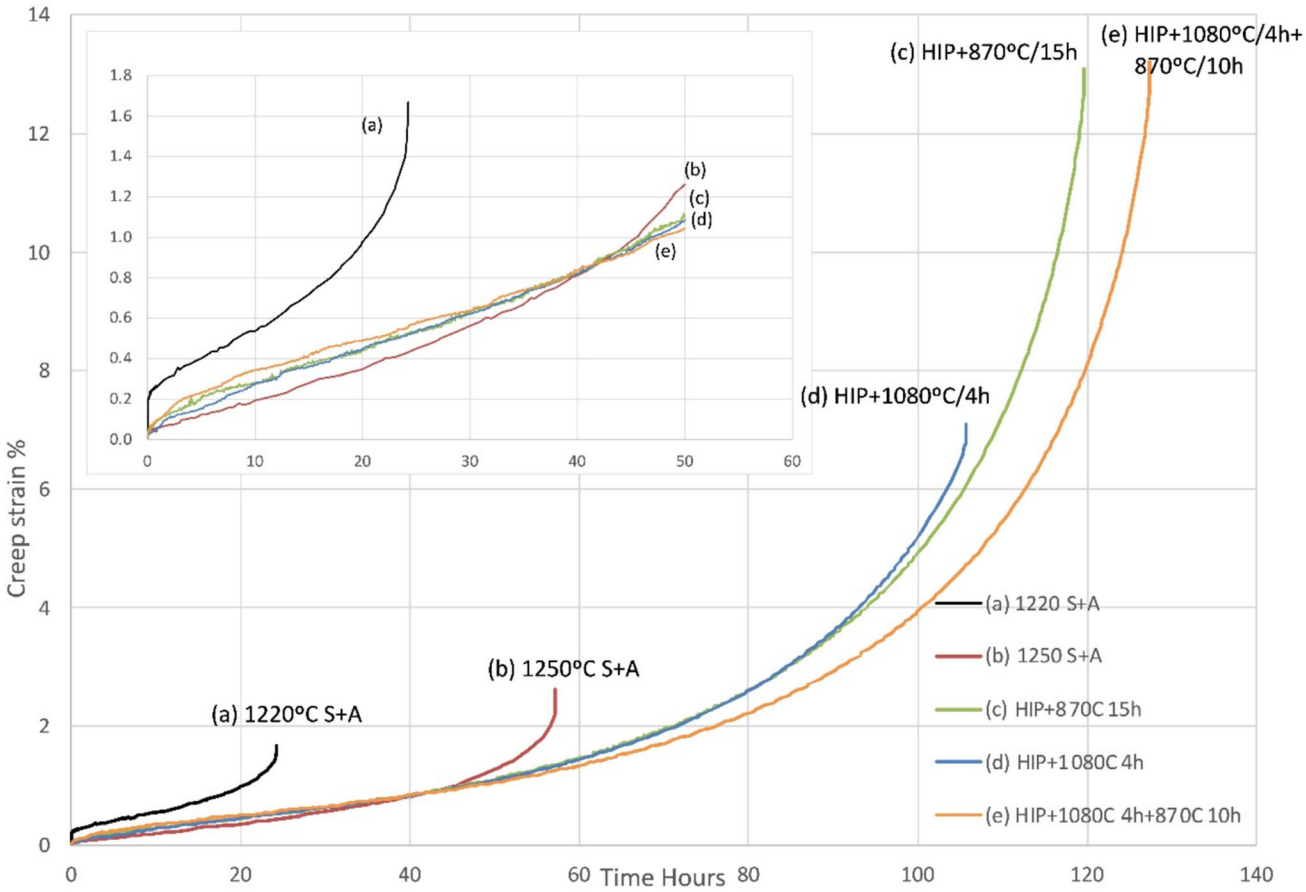

Fig. 9—Creep curve at 982 ºC/179.3 MPa of several heat-treated samples, tested in build direction. (*a*) 1220 °C/2 h + 1080 °C/4 h + 870 °C/ 20 h, (*b*)1250 °C/2 h + 1080 °C/4 h + 870 °C/20 h, (*c*) HIP + 870 °C/1 5 h, (*d*) HIP + 1080 °C/4 h, (*e*) HIP + 1080 °C/4 h + 870 °C/10 h. Insert shows the first 50 h of creep.

The HIP is important for creep as evidenced by the very poor creep lives of both samples which were not HIPed. For the Z direction, this is due to the very low elongation at fracture. The 1250 °C/2 h + 1080 °C/ 4 h + 870 °C/20 h sample fails at 57.2 hour with only 1.9 pct elongation. However, the early creep performance of this sample is excellent and out-performs all the other tests at this early stage as you might expect from the regular single crystal type microstructure optimized for creep performance, Figure 5(b). The sample fails because of cavitation on the short boundaries perpendicular to the stress axis. For all the XY samples without a HIP, the creep life is around 4 hour. HIPing improves this to over 30 hour but this is still less

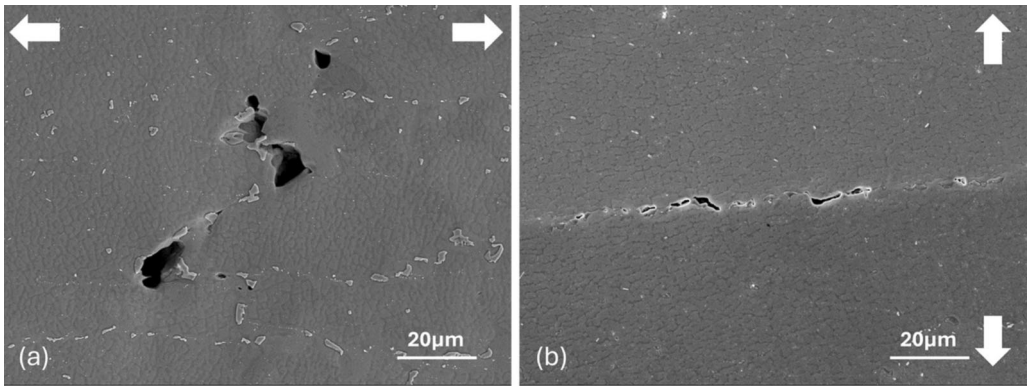

Fig. 10—SEM micrograph of failed creep samples tested at 950 °C/137 MPa, (*a*) in the Z direction and in the (*b*) XY direction. Heat treatment: HIP + 1080 °C/4 h + 870 °C/10 h. Voids can be seen in the boundaries perpendicular to the stress axis in each case. Arrows indicate the tensile axis.

than one third of the lives achieved by the Z-orientated samples. Thus, failure is caused principally by the un-healed porosity of the AM build, exacerbated by the high density of perpendicular boundaries in the XY samples.

Focussing on the tests with the tensile axis in the build direction, Z, the creep curves of the three HIPed samples in Table IV and Figure 9 are very similar, particularly in the early stages and well within the experimental scatter observed in creep tests. It is significant that this unconventional HIPed microstructure works as well as it does for these alloys, the creep rate being only slightly faster than the 1250 °C solution treatment with a more conventionally creep-resistant microstructure (Figure 9, sample (b), 1250 °C/2 h + 1080 °C/4 h + 870 °C/20 h). The HIP prevents early fracture and comparing these results with the DS-CM247LC, the longer creep life of the latter can be attributed to the large elongation to fracture.

Creep performance here is very insensitive to post-HIP heat treatment, but the HIP is essential to prevent early failure from porosity. It is worth noting that the large primary γ' gives such good creep properties. Failure of the XY samples is caused by the cavitation of the higher density of grain boundaries perpendicular to the stress axis, as shown in Figure 10, but early performance is in line with the Z-orientated samples.

V. CONCLUSIONS

The omission of the solution treatment in this alloy gives very promising tensile and creep properties but a radically different microstructure. The slow cool from the HIP determines the large scale of the primary precipitates which are spaced at about 2 μm. Subsequent annealing at 1080 °C removes the smaller precipitates between the primary γ' and reduces the volume fraction. Cooling from this temperature gives a nanoscale distribution of γ' in the gamma which is coarsened by further anneals at 870 °C. The optimum combination of these two heat treatments gives a high-volume fraction of the γ phase containing peak-aged small secondary precipitates of γ'.

This microstructure has tensile properties that match those from cast materials very well, without compromising the creep performance at low strain. The HIP treatment is essential to prevent premature failure limiting creep performance. Now the role of heat treatments applied to HIPed microstructures is understood; further optimization of the proof stress and creep strength, consistent with the production and use of additively manufactured CM247LC, is possible. For example, raising the first annealing temperature above 1080 °C and reducing slightly the duration of the second might achieve a higher yield stress, possible at the expense of ductility.

ACKNOWLEDGMENTS

This work was carried out and funded by NTT Data XAM Technologies Corporation in Osaka, and additional work at the University of Shimane was supported by the grant for fundamental research of the Next Generation TATARA Co-Creation Centre (NEXTA), which is established with Grant-in-aid for the Promotion of Regional Industries from Cabinet Office, Japan, and Shimane Prefecture.

CONFLICT OF INTEREST

On behalf of all authors, the corresponding author states that there is no conflict of interest.

OPEN ACCESS

SUPPLEMENTARY INFORMATION

The online version contains supplementary material available at https://doi.org/10.1007/s11661-025-08106-7.

REFERENCES

1. J. Shingledecker, A. Bridges, N. Harless, R. Grylls, Z. Hussain, S. Pereira, S. Srinivasan, M. Musto, K. Kroenlein, J. Saal: Learnings in the Qualification of ABD®900AM for Turbine, Aerospace, and Energy Applications. In *Volume 7: Manufacturing Materials & Metallurgy, Microturbines, Turbochargers & Small Turbomachines, Oil & Gas Applications, Steam Turbine, Structures and Dynamics: Aerodynamics Excitation & Damping*, American Society of Mechanical Engineers, Memphis, Tennessee, 2025; p. V007T17A013. https://doi.org/10.1115/GT2025-152958.
2. J.N. Ghoussoub, P. Klupś, W.J.B. Dick-Cleland, K.E. Rankin, S. Utada, P.A.J. Bagot, D.G. McCartney, Y.T. Tang, and R.C. Reed: *Addit. Manuf.*, 2022, vol. 52, 102608. https://doi.org/10.1016/j.addma.2022.102608.
3. L. Carter, M. Attallah, and R. Reed: *Superalloys*, 2012, vol. 2012, pp. 577–85.
4. L.N. Carter: *Selective Laser Melting of Nickel Superalloys for High Temperature Applications*, Birmingham University, 2013.
5. A. Fardan, A. Fazi, R.L. Peng, T. Mishurova, M. Thuvander, G. Bruno, H. Brodin, and E. Hryha: *Materialia*, 2024, vol. 34, 102059. https://doi.org/10.1016/j.mtla.2024.102059.
6. M. Gerstgrasser, M. Cloots, J. Stirnimann, and K. Wegener: *J. Mater. Process. Technol.*, 2021, vol. 289, 116948. https://doi.org/10.1016/j.jmatprotec.2020.116948.
7. Y.T. Tang, C. Panwisawas, J.N. Ghoussoub, Y. Gong, J.W.G. Clark, A.A.N. Németh, D.G. McCartney, and R.C. Reed: *Acta Mater.*, 2021, vol. 202, pp. 417–36. https://doi.org/10.1016/j.actamat.2020.09.023.
8. S. Kou: *Acta Mater.*, 2015, vol. 88, pp. 366–74. https://doi.org/10.1016/j.actamat.2015.01.034.
9. A.T. Clare, R.S. Mishra, M. Merklein, H. Tan, I. Todd, L. Chechik, J. Li, and M. Bambach: *J. Mater. Process. Technol.*, 2022, vol. 299, 117358. https://doi.org/10.1016/j.jmatprotec.2021.117358.
10. G.L. Erickson, K. Harris, and R.E. Schwer: *Directionally Solidified DS CM 247 LC Optimized Mechanical Properties Resulting From Extensive y' Solutioning*, ASME, Houston, 1985. https://doi.org/10.1115/85-GT-107.
11. J.F.S. Markanday, K.A. Christofidou, J.R. Miller, E.R. Livera, N.G. Jones, E.J. Pickering, W. Li, Y. Pardhi, C.N. Jones, and H.J. Stone: *Metall. Mater. Trans. A*, 2023, vol. 54(5), pp. 1758–75. https://doi.org/10.1007/s11661-022-06939-0.
12. S. Griffiths, H. Ghasemi Tabasi, T. Ivas, X. Maeder, A. De Luca, K. Zweiacker, R. Wróbel, J. Jhabvala, R.E. Logé, and C. Leinenbach: *Addit. Manuf.*, 2020, vol. 36, 101443. https://doi.org/10.1016/j.addma.2020.101443.
13. P. Hu, Z. Liu, M. Chen, Y. Li, X. Qi, and J. Xie: *J. Market. Res.*, 2024, vol. 29, pp. 3074–88. https://doi.org/10.1016/j.jmrt.2024.02.082.
14. J.-U. Lee, Y.-K. Kim, S.-M. Seo, and K.-A. Lee: *Mater. Sci. Eng. A*, 2022, vol. 841, 143083. https://doi.org/10.1016/j.msea.2022.143083.
15. E. Bassini, A. Sivo, P.A. Martelli, E. Rajczak, G. Marchese, F. Calignano, S. Biamino, and D. Ugues: *J. Alloy. Compd.*, 2022, vol. 905, 164213. https://doi.org/10.1016/j.jallcom.2022.164213.
16. M. Vilanova, F. Garciandia, S. Sainz, D. Jorge-Badiola, T. Guraya, and M. San Sebastian: *J. Mater. Process. Technol.*, 2022, vol. 300, 117398. https://doi.org/10.1016/j.jmatprotec.2021.117398.
17. P.A. Martelli, E. Bassini, and D. Ugues: *Prog. Addit. Manuf.*, 2025, vol. 10(1), pp. 605–18. https://doi.org/10.1007/s40964-024-00645-6.
18. A. Fardan, J. Gårdstam, E. Oscarsson, H. Brodin, and E. Hryha: *Adv. Eng. Mater.*, 2025, https://doi.org/10.1002/adem.202500691.
19. V.D. Divya, R. Muñoz-Moreno, O.M.D.M. Messé, J.S. Barnard, S. Baker, T. Illston, and H.J. Stone: *Mater Charact*, 2016, vol. 114, pp. 62–74. https://doi.org/10.1016/j.matchar.2016.02.004.
20. X. Wang, L.N. Carter, B. Pang, M.M. Attallah, and M.H. Loretto: *Acta Mater.*, 2017, vol. 128, pp. 87–95. https://doi.org/10.1016/j.actamat.2017.02.007.
21. V. Kalyanasundaram, A. De Luca, R. Wróbel, J. Tang, S.R. Holdsworth, C. Leinenbach, and E. Hosseini: *Addit. Manuf. Lett.*, 2023, vol. 5, 100119. https://doi.org/10.1016/j.addlet.2022.100119.
22. S. Griffiths, H. Ghasemi-Tabasi, A. De Luca, J. Pado, S.S. Joglekar, J. Jhabvala, R.E. Logé, and C. Leinenbach: *Mater Charact*, 2021, vol. 171, 110815. https://doi.org/10.1016/j.matchar.2020.110815.
23. R.A. Ricks, A.J. Porter, and R.C. Ecob: *Acta Metall.*, 1983, vol. 31(1), pp. 43–53. https://doi.org/10.1016/0001-6160(83)90062-7.
24. T. Grosdidier, A. Hazotte, and A. Simon: *Mater. Sci. Eng. A*, 1998, vol. 256(1–2), pp. 183–96.
25. H.-E. Huang and C.-H. Koo: *Mater. Trans.*, 2004, vol. 45(2), pp. 562–68. https://doi.org/10.2320/matertrans.45.562.
26. G.L. Drew, R.C. Reed, K. Kakehi, C.M.F. Rae: Single Crystal Superalloys: The Transition from Primary to Secondary Creep. In *Superalloys 2004 (Tenth International Symposium)*, TMS, 2004, pp. 127–136. https://doi.org/10.7449/2004/Superalloys_2004_127_136.
27. K. Kakehi: *Mater. Sci. Eng. A*, 2000, vol. 278(1–2), pp. 135–41. https://doi.org/10.1016/S0921-5093(99)00579-1.
28. D.M. Collins, R.K. Heenan, and H.J. Stone: *Metall. Mater. Trans. A*, 2011, vol. 42(1), pp. 49–59. https://doi.org/10.1007/s11661-010-0466-1.